JGR Space Physics

RESEARCH ARTICLE
10.1029/2019JA026536

Mapping the Lunar Wake Potential Structure With ARTEMIS Data

Shaosui Xu[1], Andrew R. Poppe[1], Jasper S. Halekas[2], David L. Mitchell[1], James P. McFadden[1], and Yuki Harada[3]

[1]Space Sciences Laboratory, University of California, Berkeley, CA, USA, [2]Department of Physics and Astronomy, University of Iowa, Iowa City, IA, USA, [3]Department of Geophysics, Kyoto University, Kyoto, Japan

Key Points:
- Lunar wake potentials derived from ARTEMIS data are statistically analyzed for the first time and vary with v_{sw} and T_e as expected
- A 2-D analytic model of the wake potential for a tilted IMF is developed and predicts an asymmetry potential structure, agreeing with data
- SW electron strahl causes a net potential difference across the lunar wake, suggesting potentials extending farther than previously thought

Correspondence to:
S. Xu,
shaosui.xu@ssl.berkeley.edu

Citation:
Xu, S., Poppe, A. R., Halekas, J. S., Mitchell, D. L., Mcfadden, J. P., & Harada, Y. (2019). Mapping the lunar wake potential structure with ARTEMIS data. *Journal of Geophysical Research: Space Physics*, *124*. https://doi.org/10.1029/2019JA026536

Received 22 JAN 2019
Accepted 14 APR 2019
Accepted article online 23 APR 2019

Abstract The refilling of the lunar wake is relatively well explained by the theory of 1-D plasma expansion into a vacuum; however, the field-aligned wake potential is not a directly measured quantity, and thus, a statistical analysis of wake potentials at high altitudes has not been previously performed. In this study, we obtain the wake potential by comparing the field-aligned electron distributions inside and outside of the lunar wake measured by the two probes of the Acceleration, Reconnection, Turbulence, and Electrodynamics of Moon's Interaction with the Sun (ARTEMIS) mission. The derived potentials from ARTEMIS data vary with solar wind electron temperature and bulk flow velocity as the theory predicts. We also expand the 1-D plasma theory to 2-D in the plane of the interplanetary magnetic field and the solar wind velocity to examine how a tilted interplanetary magnetic field affects the wake potential structure. As the expansion time for the two sides of the wake differs, a wake potential asymmetry is developed in our model. This asymmetry is confirmed by the data-derived wake potentials. Moreover, ambipolar electric fields are obtained from both the modeled and data-derived wake potentials and show good agreement. Lastly, we examine the effects of the solar wind strahl-electron population on the wake potential structure, which appears to cause a net potential difference across the lunar shadow. This may imply that the disturbance of the wake plasma expansion extends farther outside the wake than previous plasma-expansion theories have predicted.

1. Introduction

The terrestrial Moon can be considered as an airless and unmagnetized body to first order in terms of the interaction with the solar wind, since there is no intrinsic global magnetic field or significant ionosphere to deflect the solar wind. Thus, no traditional bow shock is formed and the interplanetary magnetic field (IMF) penetrates through the body mostly undisturbed (e.g., Colburn et al., 1967; Ness et al., 1968; Russell et al., 2016). The terrestrial Moon presents a physical obstacle to the solar wind plasma flow, and a vacuum is formed immediately behind the body. As the solar wind passes the body, it refills the wake due to the pressure gradient across the wake boundary. This refilling process produces a rarefaction wave propagating outward into the undisturbed plasma, particle expansion into the vacuum with a velocity characterized by the ion acoustic speed, exponentially decreasing plasma density into the wake, and a negative potential arising from the polarization electric field, due to the electron pressure gradient (e.g., Gurevich et al., 1969; Gurevich & Pitaevskii, 1975). Halekas et al. (2014) extended the work of Gurevich et al. (1969) and Gurevich and Pitaevskii (1975) for various plasma distributions, which were shown to match better with observations from the Acceleration, Reconnection, Turbulence, and Electrodynamics of Moon's Interaction with the Sun (ARTEMIS) spacecraft (Angelopoulos, 2011). Meanwhile, Zhang et al. (2012) demonstrated that the wake expanded outward with fast magnetohydrodynamic (MHD) wave velocities, rather than the ion acoustic speed, with ARTEMIS data. This finding fits better with an MHD description than with the simple gas dynamics theory.

The lunar wake has been observed by many spacecraft, such as the Explorer 35 and the Apollo subsatellites (e.g., Ness, 1972; Schubert & Lichtenstein, 1974, and references therein), the Wind spacecraft (e.g., Farrell et al., 1998; Ogilvie et al., 1996), Lunar Prospector (e.g., Halekas et al., 2005, 2011a), Kaguya (e.g., Nishino et al., 2009a, 2009b, 2010), Chandrayaan-1 (e.g., Dhanya et al., 2013, 2016; Futaana et al., 2010), and ARTEMIS (e.g., Halekas et al., 2011b; Poppe et al., 2014; Xu et al., 2017; Zhang et al., 2012, 2014). Plasma distributions from 1-D plasma expansion theories have also been successfully compared with observations

from Wind (e.g., Ogilvie et al., 1996), Lunar Prospector (e.g., Halekas et al., 2005, 2011a), Chandrayaan (e.g., Futaana et al., 2010; Hutchinson, 2013), ARTEMIS (e.g., Halekas et al., 2011b, 2014), and Chang'E (e.g., Wang et al., 2010). The lunar wake properties, such as the magnetic field strength and plasma density and temperature (and consequently the plasma and magnetic pressure), have been statistically mapped with ARTEMIS data (Zhang et al., 2014). An array of sophisticated numerical models have also been used to simulate the Sun-Moon interaction, such as Vlasov simulations (e.g., Umeda et al., 2011), MHD simulations (e.g., Harnett & Winglee, 2002; Xie et al., 2013), hybrid simulations (e.g., Fatemi et al., 2013, 2017; Holmström et al., 2012; Kallio, 2005; Trávnícek et al., 2005; Wang et al., 2011; Wiehle et al., 2011), and particle-in-cell simulations (e.g., Birch & Chapman, 2002; Farrell et al., 1998; Kimura & Nakagawa, 2008; Nakagawa, 2013).

The lunar wake electrostatic potential, ϕ, however, cannot be directly measured. Halekas et al. (2011b) devised a method to obtain the wake potential by comparing the field-aligned electron phase space density distributions inside and outside of the wake, assuming steady solar wind conditions, for the first lunar wake crossing made by the ARTEMIS probe P1. The wake potential from ARTEMIS observations agrees relatively well with the 1-D plasma expansion theory (equation (1)); however, there exists a disparity in the wake potential obtained from the inbound pass to the wake and outbound, not explained by the theory but attributed to the asymmetry (caused by the strahl population) in the solar wind electron distribution. In this study, we expand this methodology to six years of ARTEMIS observations, from late 2011 to the end of 2018, to statistically investigate the lunar wake potential structure. Furthermore, many previous theories on the 1-D plasma expansion assume that the IMF is perpendicular to the solar wind velocity. The effect of a non-perpendicular IMF on the lunar wake was considered by Halekas et al. (2011b) and Halekas et al. (2014). Here, we theorize that a tilted IMF, neither perpendicular nor parallel to the solar wind flow, can also lead to an asymmetry in the wake potential structure. These two factors, an asymmetry in the solar wind electron distribution and a tilted IMF, are examined separately with regard to their effects on the wake potential asymmetry with ARTEMIS data.

2. Plasma Expansion Theory for a Tilted IMF

The refilling of the lunar wake is usually considered as a process of a plasma expanding into a vacuum, first theorized with several assumptions, such as quasi-neutrality and self-similarity (i.e., assuming a space $[S]$-time $[t]$-dependent solution $[S/t]$ for plasma density and velocity), by Gurevich et al. (1969) and Gurevich and Pitaevskii (1975). With these assumptions, analytical solutions for the potential ϕ, ion velocity v_i, and the relative density n/n_0, can be obtained by assuming a single species and a cold Maxwellian ion distribution (e.g., Ogilvie et al., 1996; Samir et al., 1983), as,

$$\phi = -(T_e/e)(S/(C_s t) + 1); S/(C_s t) + 1 \geq 0, \tag{1}$$

$$v_i = C_s[S/(C_s t) + 1], \tag{2}$$

$$n/n_0 = \exp(\frac{\phi}{T_e/e}) = \exp[-(S/(C_s t) + 1)], \tag{3}$$

where n is the local density, n_0 is the undisturbed plasma density outside of the vacuum, $C_s = \sqrt{T_e/M_i}$ is the ion acoustic speed, T_e is the electron temperature in energy units, and M_i is the ion mass. S is the distance that the plasma travels along the magnetic field line, and t is the expansion time. Equations (2) and (3) also assume ions to be singly charged.

The aforementioned self-similar solutions (equations (1)–(3)) assume no plasma entry from the other side of the vacuum. To take into account two opposite ion streams entering the lunar wake, Hutchinson (2012) derived an analytical solution for when the IMF is perpendicular to the solar wind velocity V_{sw} with an axial symmetry relative to the solar wind velocity using the following methodology: (1) potentials for each side of the wake, say ϕ_1 and ϕ_2, are obtained following equation (1); (2) the ion density from each side, n_1 and n_2, can then be derived with ϕ_1 and ϕ_2 following equation (3); (3) the total density is approximated by $n_{\text{total}} = n_1 + n_2$, which is (4) then used to rederive the final potential ϕ with equation (3). In this section, following similar steps, we construct an analytical solution for a tilted IMF, that is, IMF neither perpendicular nor parallel to V_{sw}.

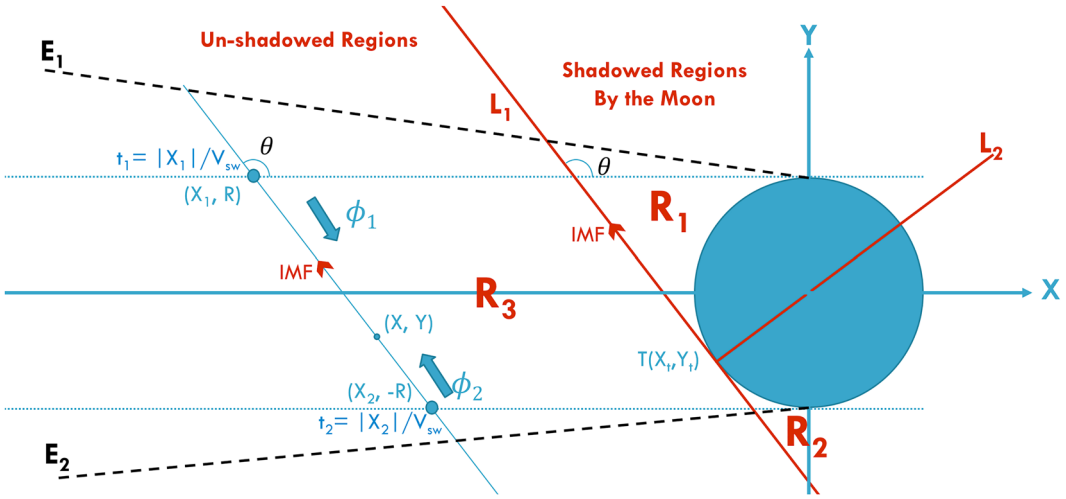

Figure 1. Geometry for a tilted interplanetary magnetic field (IMF): In a 2-D plane, the X axis points opposite the solar wind flow velocity, and the Y axis is parallel to the perpendicular component of the IMF with respect to the X axis. The IMF has an angle of $\theta = \arccos(B_x/|B|)$ with the X axis. A boundary line L_1 separates regions magnetically connected (R1 and R2) and unconnected (R3) by the Moon, which is parallel to the IMF and intersects the lunar surface at a tangent point $T(X_t, Y_t)$. The two shadowed regions, R1 and R2, are divided by another boundary line L_2, which connects T and the center of the Moon. E_1 and E_2 represent the expansion fronts of the rarefaction waves on each side. Then, at an observation point (x, y), the IMF intersects $Y = \pm 1\,R$ at (X_1, R_L) and $(X_2, -R_L)$, where R_L is the lunar radius.

Figure 1 illustrates the geometry for a tilted IMF, which has an angle of $\theta = \arccos(B_x/|B|)$ with the X axis. There are three distinct regions: two regions magnetically connected to the Moon (R1 and R2) and an unobstructed region (R3), separated by L_1 and L_2. For an observation point (x, y) within R1, there is only plasma expanding from $Y = R_L$ to the lunar surface, and thus, the potential, ϕ_1, is given by the 1-D plasma theory (equations (1)–(3)):

$$\phi_1/(T_e/e) = -1 - \frac{1}{u}\frac{R_L - y}{x\sin\theta + (R_L - y)\cos\theta}, \tag{4}$$

where $u = C_s/V_{sw}$. We assume no reflected plasma from the lunar surface potential (e.g., Halekas et al., 2002, 2011a; Whipple, 1981) or from lunar crustal magnetic fields. Similarly, for an observation point (x, y) within R2, there is only plasma expanding from $Y = -R_L$ to the lunar surface, and thus, the potential ϕ_2 is

$$\phi_2/(T_e/e) = -1 - \frac{1}{u}\frac{R_L + y}{x\sin\theta - (R_L + y)\cos\theta}. \tag{5}$$

Note that equations (4) and (5) revert to equation (3) for $\theta = 90°$.

For an observation point (x, y) within R3, plasma enters from both sides of the wake. Following the four steps listed above, the potential, ϕ_3, can be derived as

$$\phi_3/(T_e/e) = -1 + \ln\left\{\exp\left[-\frac{1}{u}\frac{R_L - y}{x\sin\theta + (R_L - y)\cos\theta}\right] + \exp\left[-\frac{1}{u}\frac{R_L + y}{x\sin\theta - (R_L + y)\cos\theta}\right]\right\}. \tag{6}$$

A detailed derivation for equations (4)–(6) is presented in the appendix. Note that these solutions are only valid within the expansion fronts (E_1 and E_2)

We note that the methodology described above is not entirely self-consistent for R3, which introduces some complication. Initially, for step 1, the zero-potential reference is at the expansion fronts E_1 and E_2 (see equations (A7) and (A10)). By adding n_1 and n_2 together (step 3), the derived final potential (step 4) is no longer zero at E_1 and E_2. For the axial-symmetric scenario in Hutchinson (2012), one only needs to subtract the potential at the expansion fronts, which is the same for E_1 and E_2, from the final potential. For the asymmetric situation here, however, the analytical expressions of potentials within R3 at E_1 and E_2 are not the same (as expected), which implies that the expansion front at one side is more perturbed than the other

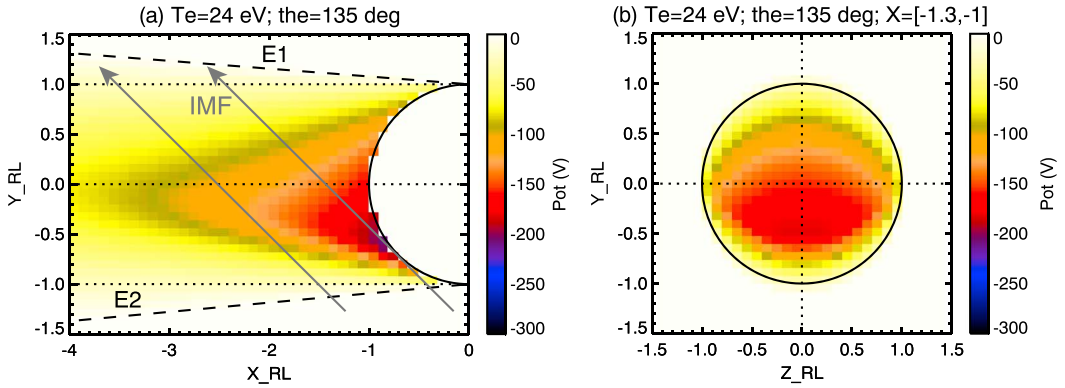

Figure 2. (a) The wake potential calculated from equations (4)–(6) for $R1$, $R2$, and $R3$ combined, with a solar wind speed of $|V_{sw}| = 400$ km/s, an electron temperature of $T_e = 24$ eV, and an IMF angle of $\theta = 135°$. (b) The averaged potential from our theory in the Y-Z plane for $X = [-1.3, -1.0]$. (c) The potentials at the expansion fronts E_1 and E_2. IMF = interplanetary magnetic field.

side. Nonetheless, under nominal solar wind conditions, equation (6) gives $\phi/(T_e/e) \ll 1$ at E_1 and E_2 (i.e., the corrections are negligible), and therefore, we do not apply any corrections here.

Figures 2a and 2b illustrate the analytical potential from equations (4)–(6) in the x-y and y-z planes, respectively, for $|V_{sw}| = 400$ km/s, $T_e = 24$ eV, and $\theta = 135°$. The typical solar wind electron temperature is around 12 eV for the core population, but the energy density integrating over the entire solar wind electron distribution is roughly twice of the core population; thus, T_e =24 eV is used here for a better comparison with observations in section 4. Moreover, suprathermal electrons should contribute to the potential structure more significantly deep in the wake, as the core electrons do not penetrate very far into the wake. A few physical insights can be obtained from these two figures. First, an obvious wake potential asymmetry is present in Figure 2a, more negative on the $-Y$ side, arising from a shorter expansion time from the $-Y$ side ($t_1 = X_1/V_{sw}$, as shown in Figure 1) than at the $+Y$ side ($t_2 = X_2/V_{sw}$) so that the $+Y$ side has a longer relaxing time and thus shallower potentials. Second, the calculated potential on the expansion fronts, without corrections, is almost 0 (not shown), suggesting the disturbance from plasma entry from the opposite side is negligible. In other words, only a very small portion of the plasma from one side penetrates through the wake and exits from the other side. Third, although potentials in Figure 2a are obtained with three different solutions (equations (4)–(6)), no sharp transition exists among these three regions (R1–R3). This is again because the perturbation to one side of the wake from plasma entry from the opposite side is insignificant so that equation (6) is effectively the same as equation (4) or (5) at each side, that is, effectively only having plasma entry from one side. However, the separation of the two sides of the wake for R3, or the minimum potential across the wake, is naturally determined by equation (6).

3. Orbit Example

Now that we have established that a tilted IMF should lead to an asymmetric wake potential structure from a theoretical point of view, we now test this theory with observations. Halekas et al. (2011b) obtained the wake potential during the first lunar wake passing made by ARTEMIS probe P1 by comparing the field-aligned electron phase space density distributions inside and outside of the wake, assuming steady state solar wind conditions. To illustrate this technique, we take an orbit of ARTEMIS probe P1 on 1 January 2014 as an example, as shown in Figure 3. The spacecraft entered the wake at around 08:13 UT and exited at around 08:52 UT (Figure 3a). The magnetic field is relatively steady within and outside of the wake (Figures 3b and 3c), suggesting steady upstream conditions. The SSE coordinates are defined as follows: the X axis points opposite to the solar wind flow velocity, the Y axis points opposite to the Moon's orbital motion, and the Z axis completes the right-handed system.

The energy spectrograms for parallel (Figures 3f) and antiparallel (Figures 3g) electrons, corrected for spacecraft potentials, show a decrease in electron fluxes in the wake, in particular at low energies, as electrons are decelerated and/or reflected by the wake potential. By assuming steady state solar wind conditions, the change in electron fluxes is considered to be solely caused by the wake ambipolar potential, which can thus

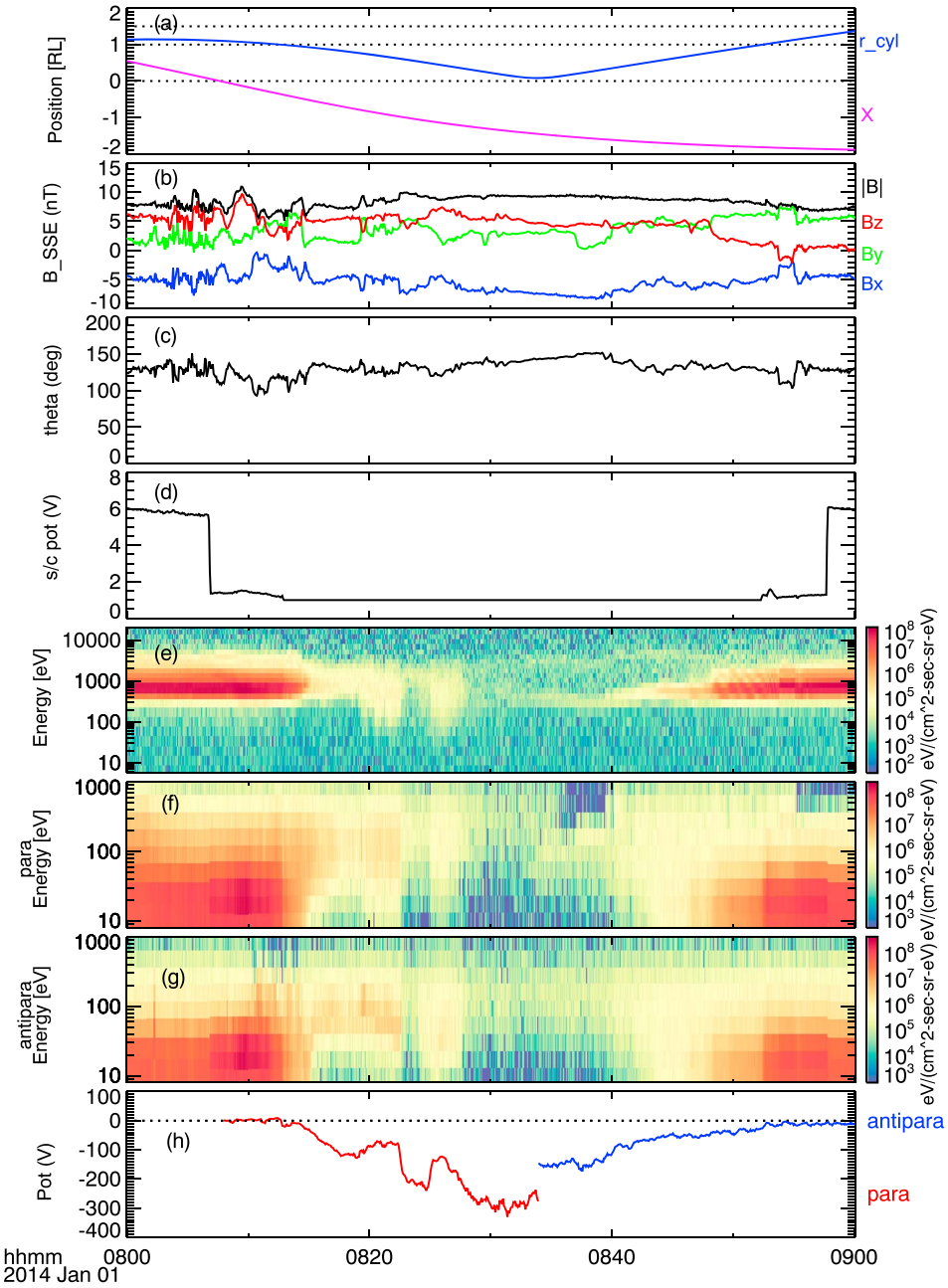

Figure 3. An ARTEMIS probe P1 orbit example on 1 January 2014. From top to bottom, the time series of (a) the spacecraft position in the cylindrical coordinates, where the X axis points opposite to the solar wind flow velocity, r_{cyl} is the distance from the X axis; (b) the magnetic field strength and vector components in the SSE coordinates; (c) the magnetic angle relative to the X axis; (d) the spacecraft potential; (e) the averaged ion energy spectra; (f) and (g) the electron energy flux for pitch angles 0–15° and 165–180°, respectively, both corrected for spacecraft potentials; and (h) the deduced wake potential from electrons traveling toward the wake, parallel electrons for inbound (red) and antiparallel electrons for outbound (blue).

be obtained by comparing electron phase space density distributions inside and outside of the lunar wake. As the zero potential is set to be outside of the wake, the potentials obtained from 40- to 500-eV electrons traveling toward the wake from both sides, that is, parallel electrons for inbound (red) and antiparallel electrons for outbound (blue), are shown in Figure 3h. Electrons' motion with respect to the wake, entering or exiting, is determined from a combination of the spacecraft position, the magnetic field direction, and electron pitch angles.

The potential stays near zero outside of the wake, as expected, and decreases rapidly toward the wake center. The minimum potential reaches roughly −300 V for inbound and −150 V for outbound. A disparity of ~150 V in the minimum potential for inbound and outbound is seen, similar to the case study in Halekas et al. (2011b). The parallel electrons have a higher flux at energies ~50–600 eV than that of antiparallel electrons outside of the wake (07:56–08:10 UT), suggesting a strahl population (Figures 3f and 3g). As discussed in Halekas et al. (2011b), an asymmetry in electron distributions (from this strahl population) entering from each side of the wake leads to an asymmetry in the wake potential structure. Alternatively, we consider the effective electron temperature of parallel electrons to be higher than that of antiparallel electrons, which results in a larger potential difference for the inbound segment. Meanwhile, the IMF has an angle of ~135° with the X axis (Figures 3c), which might cause some asymmetry in the wake potential as well. Finally, we also note that the presence of excess electrons and apparent steps in the derived electrostatic potential between times of 8:19–8:23 and 8:25–8:28 UT, corresponding to high ion fluxes in Figure 3e. We interpret it as solar wind protons being reflected from crustal magnetic anomalies on the lunar dayside (e.g., Nishino et al., 2009a) and shortening the potential drop in the wake. Our methodology for calculating the electrostatic potentials captures the local decrease in potential magnitude caused by the presence of these protons, which serve to locally attract electrons along the field lines.

4. Statistical Mapping With ARTEMIS Data

This method of comparing electron phase space density distributions inside and outside of wake can be applied to a large time range of ARTEMIS data to obtain the average wake potential. We then statistically analyze the wake potential structures, in particular the controlling factors of the wake potential asymmetry. The ARTEMIS mission consists of two probes, P1 and P2, with comprehensive plasma and fields instrumentation orbiting the Moon in elliptical orbits (Angelopoulos, 2011). The main data sets involved are electron data from the electrostatic analyzer (McFadden et al., 2008) and magnetic field data from the fluxgate magnetometer (Auster et al., 2008) collected by each probe (P1 and P2) from 29 June 2011 to 31 December 2018.

4.1. Data Selection

The region of interest is when the Moon is immersed in the solar wind, upstream of the Earth's bow shock. We use an average bow shock fit from Chao et al. (2002) to select when the Moon is located in the solar wind but replace the nose of the bow shock from 13 R_e (Earth radius) to 15 R_e to allow for a buffer for bow shock movements in response to upstream variations. Note that we did not exclude periods when the spacecraft in the foreshock region, as we expect the perturbation from the foreshock ions (Nishino et al., 2017) do not significantly impact our statistical analyses. Only orbits with wake crossings are selected by examining P1's and P2's positions in the SSE coordinates.

Similar to the example shown in Figure 3, the wake potential is obtained with electron measurements within PAs 0–15° and 165–180° for an energy range of 40–500 eV for each orbit that satisfies the aforementioned selection criteria. A caveat is that this energy range of 40–500 eV might not be sufficient deep in the wake, where the wake potential might be < -500 V. However, the data are very noisy at high energies in the wake due to low counts and the energy resolution for high energies is also very coarse so that we choose not to use data beyond 500 eV. For each orbit, the potential tracing starts from a cylindrical distance (r_{cyl}) from the X axis in the SSE coordinates of 1.3–1.5 R_L, which is assumed to be the undisturbed solar wind and set as the zero potential, into the closest approach to the center of the wake (the smallest r_{cyl}) for inbound and outbound separately. We only use electrons traveling toward the lunar wake to obtain potentials as the reference solar wind electrons at 1.3–1.5 R_L are less likely affected by the wake potentials than electrons traveling away from the lunar wake (i.e., since exiting electrons have already traversed the opposite side of the lunar wake). All the electron data are corrected for spacecraft potentials (Halekas et al., 2011b) before being used to derive field-aligned potentials. As pointed out by Halekas et al. (2011b), the electric field instrument (Bonnell et al., 2009) onboard ARTEMIS actively controls the spacecraft potential in shadow to be less than approximately a few volts, which is much smaller than the estimated lunar wake potential. Lastly, we have not filtered out the data with wake proton entry events to ensure sufficient samplings. Protons entering the

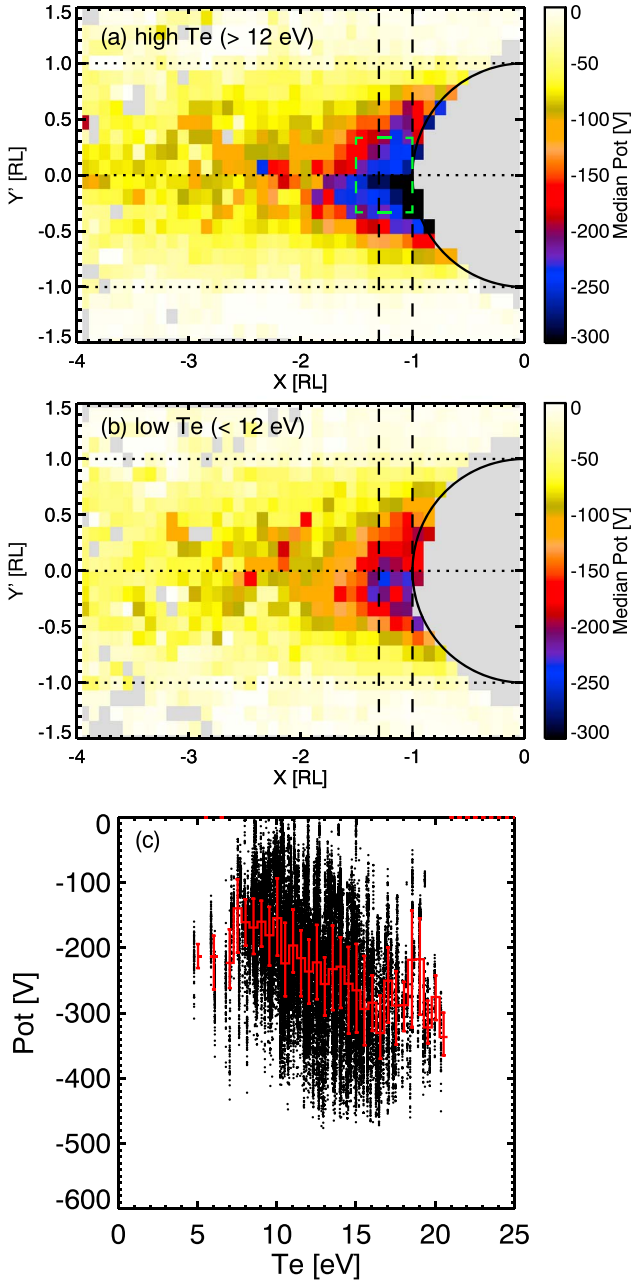

Figure 4. The map of wake potentials in the X-Y' plane in the abbreviated coordinates, averaged over $Z' = [-0.5, 0.5]$, for solar wind electron temperature (a) $T_e > 12$ eV (energy unit) and (b) $T_e < 12$ eV. The gray pixels are where there are less than 10 samples or no data, the same applied to Figures 5–11. (c) Wake potential as a function of electron temperature for $X = [-1.5, -1]$, $Y' = [-0.25, 0.25]$, and $Z' = [-0.5, 0.5]$, as indicated by the green dashed box in (a). The solid line and error bars in (c) show the quartiles of each bin.

wake happens roughly <30% of the time and at various locations so that we do not expect these events to significantly impact our results.

This methodology assumes that the solar wind electrons remain the same for the whole wake crossing, which is more likely to be the case under steady solar wind conditions. We first calculate the average upstream conditions for $r_{cyl} > 1$ for inbound and outbound separately, including the θ angle between the IMF and X_{SSE}, the clock angle of IMF (arctan[B_{ZSSE}/B_{YSSE}]), solar wind velocity, and solar wind electron temperature. We then further select orbits under a steady IMF condition, defined as variations in θ less than 60° and variations in clock angles less than 90° for inbound and outbound solar wind measurements just outside the lunar wake.

4.2. Parameter Studies

The abbreviated coordinates: to map the wake potentials, especially to investigate the asymmetry, we need to define abbreviated coordinates so that the asymmetry is not averaged out. Similar to the coordinates $[X, Y, Z]$ from our theory (Figures 1 and 2), the X axis still points at the Sun, the Y' axis is parallel or antiparallel to the perpendicular component of the IMF, and the Z' axis completes the right-handed system. More specifically, the two sets of coordinates ($[X, Y, Z]$ and $[X, Y', Z']$) are the same, $Y' = Y$ and $Z' = Z$, for the away sector IMF (i.e., $90 < \theta < 180$), but both Y and Z are both flipped, $Y' = -Y$ and $Z' = -Z$, for the toward sector IMF (i.e., $0 < \theta < 90$). In the new abbreviated coordinates $[X, Y', Z']$, the leading end of the IMF lies in $+Y'$ and the trailing end in $-Y'$ for a nominal parker spiral IMF. The benefits of such coordinates include (1) the strahl electrons always travel from $-Y'$ to $+Y'$ along the field line and (2) the IMF intersects $Y' = -R_L$ at a smaller $|X|$ than $Y' = R_L$ (in other words, a shorter relaxation time for the $-Y'$ side than the $+Y'$ side), both of which lead to a larger potential difference at the $-Y'$ side than the $+Y'$ side.

According to equation (1), the potential is directly scaled by the electron temperature T_e. We separately map the wake potentials for $T_e > 12$ eV (approximately the median value) and $T_e < 12$ eV in Figures 4a and 4b, respectively. A minimum sample number of 10 is required in each bin, otherwise shown as gray pixels in Figures 4–6, 8, and 11. The wake potential for $T_e > 12$ eV (Figure 4a) varies from near zero for $|Y'| \geq 1\,R_L$ to ~ -300 V near the center of the wake. The wake potential structure extends from $X = -0.5\,R_L$ to $X = -3.0\,R_L$ for potentials < -100 V. The potential is slightly negative for $|Y'| > 1$, because the expansion front and accompanying rarefaction region expand far along the IMF outside of the lunar shadow as the expansion time ($t = |X|/|V_{sw}|$) increases. For $T_e < 12$ eV (Figure 4b), the potential is less negative in general than the high electron temperature case, with a minimum potential of ~ -200 V. The potential is also less extended, only up to $X = \sim -2\,R_L$ for potentials < -100 V. This is in agreement with the 1-D plasma expansion theory (equations (1)–(3)), as more electrons are distributed in the high-energy tail to set up the ambipolar electric field for a higher T_e. Alternatively, we can examine how the potential varies with electron temperature within a small region ($-1.5 < X < -1$, $|Y'| < 0.25$, and $|Z'| < 0.5$), as shown in Figure 4c. The wake potential decreases roughly linearly with increasing electron temperature, as the theory predicts.

Another physical insight that can be obtained from equation (1) is that the expansion time ($= |X/V_{sw}|$) is scaled by the solar wind speed. We separately map the wake potentials for solar wind speed, $|V_{sw}| >$ 370 km/s (approximately the median value) and $|V_{sw}| <$ 370 km/s, as shown in Figures 5a and 5b,

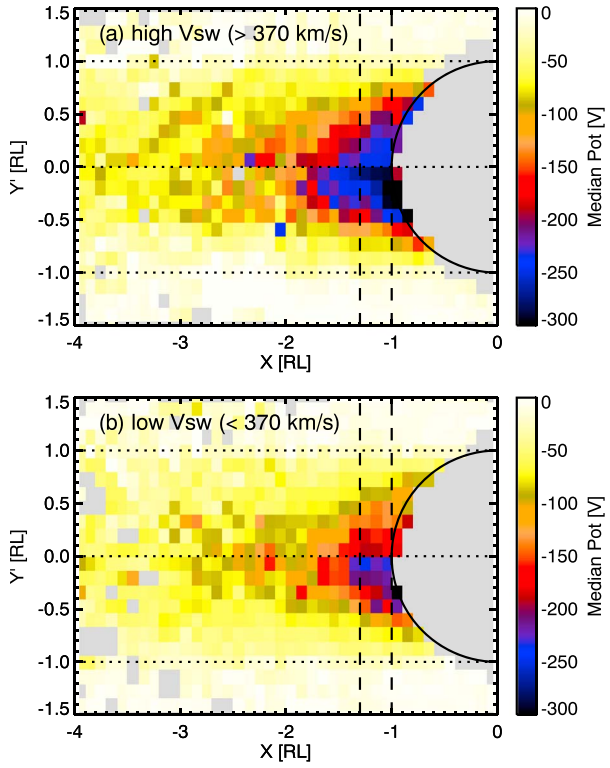

Figure 5. The map of wake potentials in the X-Y' plane in the abbreviated coordinates, averaged over $Z' = [-0.5, 0.5]$, for solar wind speed (a) $|V_{sw}| > 370$ km/s and (b) $|V_{sw}| < 370$ km/s.

respectively. The minimum potentials are ~ -300 and ~ -250 V for high and low solar wind velocities, respectively, immediately behind the Moon. The wake potential is also much more extended for the high solar wind speed case, since equivalent expansion times lead to greater downstream convection distances.

4.3. Asymmetry in Wake Potential

From Figures 4 and 5, an asymmetry in the wake potential about the X axis is seen, more negative in the $-Y'$ side, as both the presence of the strahl population and a tilted IMF lead to a larger potential difference in $-Y'$ than $+Y'$ in the abbreviated coordinates. In this section, we examine each of the two factors independently by dividing the data into cases with and without strahl and cases with parallel, perpendicular, and intermediate IMF (with respect to the solar wind flow velocity). We define the IMF cone angle to be the smaller angle between the IMF and the X axis; that is, cone = $\arccos(|B_x|/|B|)$, to determine parallel, perpendicular, and intermediate IMFs. The cone angle varies from 0° to 90°, or in other words, cone = θ for $0 < \theta < 90°$ and cone = $180 - \theta$ for $90° < \theta < 180°$ (e.g., cone = 45° in the example in Figure 2).

To determine whether there is an obvious strahl population in the solar wind electron distribution, we calculate the flux ratios (FRs) of parallel (PA 0–15°) and antiparallel (PA 165–180°) electrons for each energy bin within 80–400 eV and then obtain the averaged FR for a single measurement. FRs for all measurements outside of the wake ($|Y'| > 1\,R_L$) are averaged again separately for inbound and outbound as the representative FR. If the FR between the two field-aligned directions is above a certain threshold (A_{th}), that is, $FR > A_{th}$ or $FR < 1/A_{th}$, we define this inbound/outbound segment as a case with strahl; if $1/A_{th} < FR < A_{th}$, we define it as a case with no strahl.

4.3.1. Strahl Effects Under Perpendicular IMFs

To examine the strahl effects, we limit to cases with only perpendicular IMFs (cone angle >70°) and then map the wake potentials for cases with strahl ($FR > 2$ or $FR < 1/2$, where $A_{th} = 2$) and with no strahl ($1/2 < FR < 2$), shown in Figures 6a and 6b, respectively. An asymmetry in the potential to the X axis is observed for the strahl case for $-2 < X < 0$ (Figure 6a), more negative potentials at the $-Y'$ side. In contrast, the potential structure is more symmetric for the nonstrahl case (Figure 6b). This is in agreement with the case study in section 3 and the case study in Halekas et al. (2011b). A similar asymmetry can be

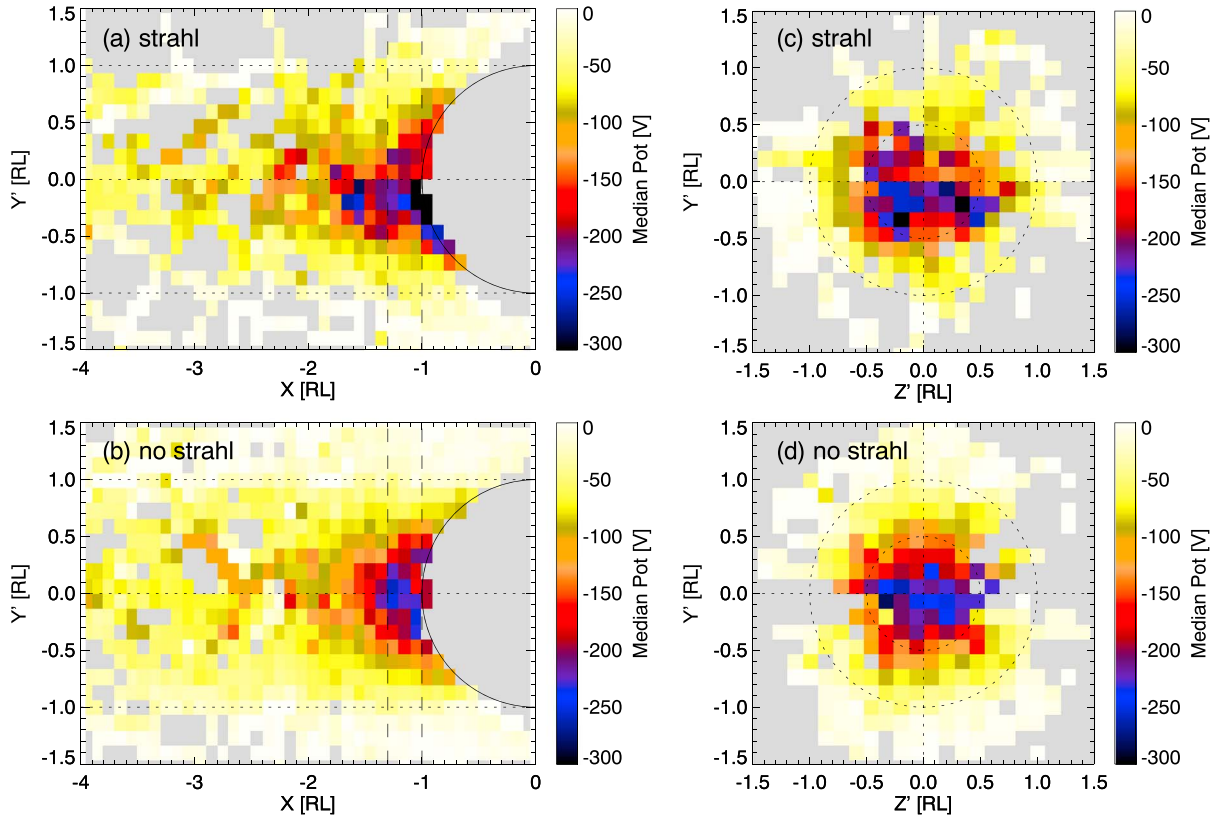

Figure 6. The maps of wake potentials in the abbreviated coordinates for perpendicular interplanetary magnetic fields (cone angle >70°): (a, b) in the X-Y' plane averaged over $Z' = [-0.5, 0.5]$; (c, d) in the Y'-Z' plane averaged over $X = [-1.3, -1.0]$ (as indicated by the two vertical dashed lines in a and b). (a) and (c) cases with strahl ($FR > 2$ or $FR < 1/2$). (b) and (d) cases with no strahl ($1/2 < FR < 2$). FR = flux ratio.

seen in Figure 6c, a projection in the Y'-Z' plane, for example, comparing $-0.5 < Y' < 0$ and $0 < Y' < 0.5$, for the strahl case but more symmetric in Figure 6d for the nonstrahl case.

Electric fields can be derived from Figures 6a and 6b by differentiating the potential in the X and Y' direction separately; that is, $E_x = -[\phi(x,y) - \phi(x - \Delta x, y)]/\Delta x$, $E_y = -[\phi(x,y) - \phi(x, y - \Delta y)]/\Delta y$, and $|E| = \sqrt{E_x^2 + E_y^2}$. We ignore the Z' component of the electric field here, as this component is supposed to be symmetric to the X-Y' plane (see Figure 2b) and should be averaged out within the X-Y' slab for $Z' < \pm 0.5$. Note that the solar wind motional electric field term is not included in the calculation. The derived electric field magnitudes and directions are shown in Figures 7a and 7b, for the strahl case and the nonstrahl case, respectively. In both cases, the electric field magnitude varies from 0 to ~0.3 mV/m, with a cone-like high values behind the planet. The electric field from each side is directed toward the X axis, mostly in the $+Y'$ or $-Y'$ direction near the wake boundary but turns side ways with an increasing E_x near the wake center. At $Y' \sim 0$, the electric field points toward the Moon. The electric field has a significant component perpendicular to the IMF in some places, for example, at $Y' \sim 0$. This perpendicular component mainly arises from the convection of the magnetic flux tube downstream. In other words, the time dependence of the refilling process results in a density gradient across the magnetic field line as IMFs convect downstream. In contrast, the Z' component of the electric field, also perpendicular to the magnetic field, is caused by the density gradient across Z', where the effective lunar radius changes with Z'.

Differences can be seen for the strahl case and the nonstrahl case. The electric field magnitude is larger in the $-Y'$ side than the $+Y'$ side for the strahl case (Figures 7a). In contrast, the magnitudes are more symmetric to the X axis for the nonstrahl case (Figures 7b). Arguably, the separation of $\pm E_y$, or where the electric field mostly in the X direction, is located at $Y' = -0.15$ for the strahl case but located at $Y' = 0$ for the nonstrahl case, more symmetric in the latter case.

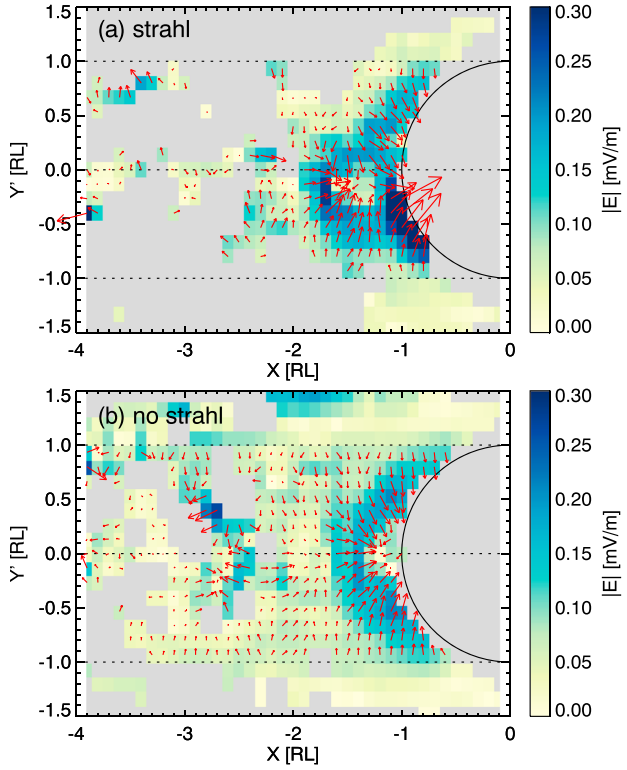

Figure 7. The maps of derived electric fields in the X-Y' plane for perpendicular interplanetary magnetic fields (cone angle >70°): (a) cases with strahl ($FR > 2$ or $FR < 1/2$) and (b) cases with no strahl ($1/2 < FR < 2$). The color shows the electric field magnitude, and the arrow indicates its direction. The arrow lengths are scaled by electric field magnitudes. FR = flux ratio.

4.3.2. IMF Effects Under No Strahl Condition

Similarly, we can examine the IMF effects by limiting the data set to nonstrahl cases ($1/2.5 < FR < 2.5$, a slightly larger threshold to allow for more samples). For all the cases with no strahl, we divide the data into three cone angle ranges: cone angle <50° (representing quasi-parallel IMF), 50° < cone angle < 75° (representing intermediate IMF), and cone angle >75 ° (representing perpendicular IMF).

The maps of wake potentials for these three categories are displayed in Figure 8. The wake potential is much more extended for more parallel IMFs (smaller cone angles), comparing Figures 8a-8c, in agreement with classic theories (e.g., Russell et al., 2016). This is due to a much longer expansion distance for more parallel IMFs. In addition, a pronounced asymmetry in the potential structure can be seen for quasi-parallel and intermediate IMFs (Figures 8a and 8b), in contrast to the symmetric wake potentials for perpendicular IMFs (Figure 8c). The results in Figure 8c (identical to Figure 6b) represent the simplest scenario, for symmetric solar wind electron distributions and a perpendicular IMF to the solar wind velocity. Figures 8d–8f show the projection in the Y'-Z' plane. Similarly, the potentials are more negative in the $-Y'$ side than the $+Y'$ side for quasi-parallel and intermediate IMF (Figures 8d and 8e) but are increasingly symmetric to the Y' axis for perpendicular IMF (Figures 8f). Finally, the potential patterns for the parallel IMF case (Figure 8a and Figure 8b) resemble our model results with a cone angle of 45° (Figures 2a and 2c), further validating our model.

The derived electric fields from Figures 8a–8c are shown in Figures 9a–9c, corresponding to quasi-parallel, intermediate, and perpendicular IMFs, respectively. Comparing these three figures, for more parallel IMFs, the electric field strength increases, probably because the refilling of the wake vacuum is harder so that the density gradient across the wake is larger. For $-2 < X < -1$, the electric field is asymmetric to the X axis for parallel and intermediate IMFs but more symmetric for perpendicular IMFs, as the difference in the expansion time for $\pm Y'$ is larger for more parallel IMFs. Meanwhile, the separation of $\pm E_y$, or where the

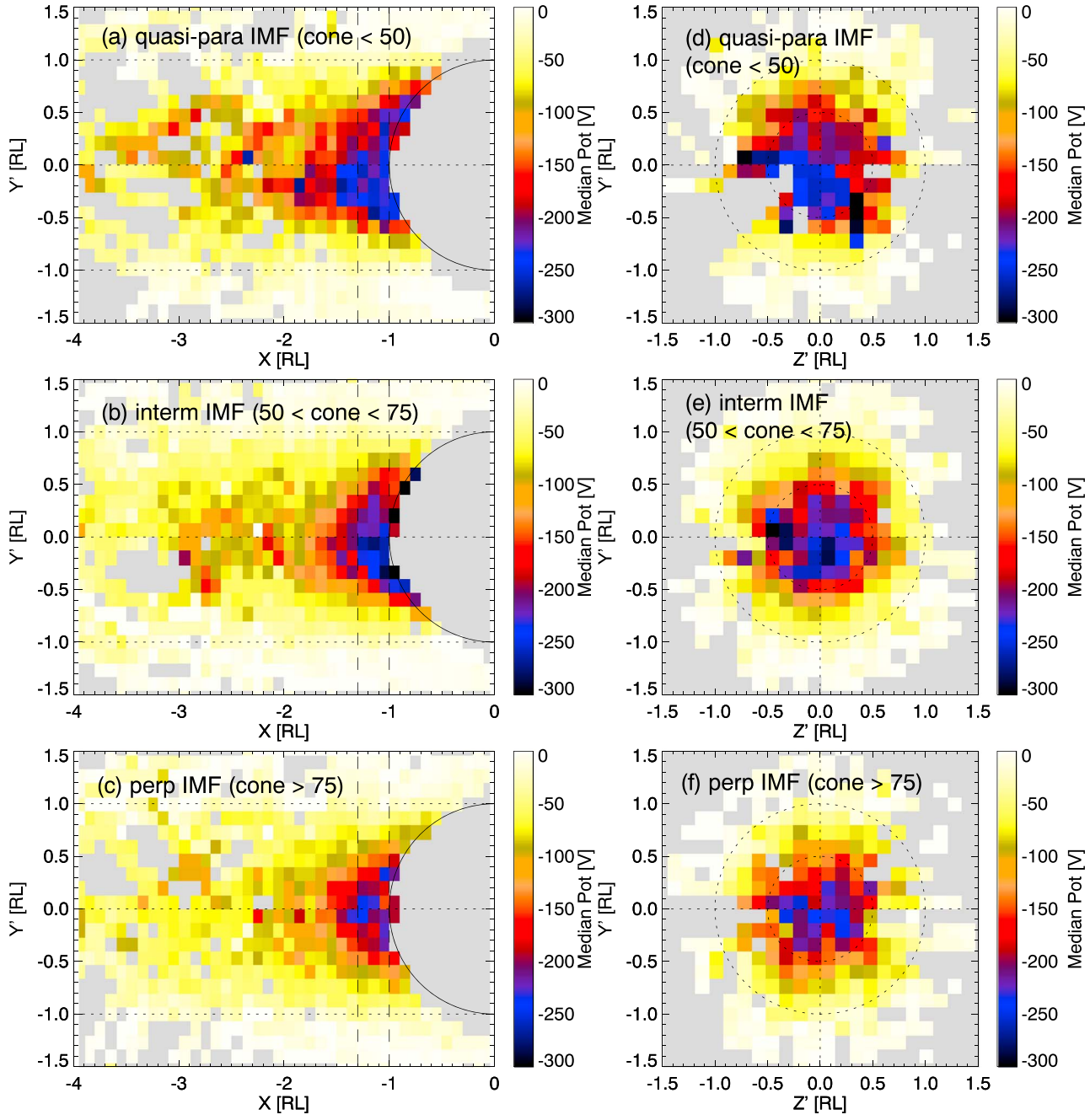

Figure 8. The maps of wake potentials in the abbreviated coordinates for cases with no strahl ($1/2.5 < FR < 2.5$): (a–c) in the X-Y' plane averaged over $Z = [-0.5, 0.5]$; (d–f) in the Y'-Z' plane averaged over $X = [-1.3, -1.0]$ (as indicated by the two vertical dashed lines in (a)–(c). (a and d) Quasi-parallel IMFs (cone angle <50°); (b and e) Intermediate IMFs (50° < cone angle < 75°); (c and f) Perpendicular IMFs (cone angle > 75°). IMF = interplanetary magnetic field.

electric field is mostly in the X direction, is located at $Y' = [-0.1, -0.2]$ for quasi-parallel and intermediate IMFs but located at $Y' = \sim 0$ for perpendicular IMFs.

4.4. Data-Model Comparison

To more quantitatively compare the modeled potentials to the data-derived potentials, we run our model with median upstream conditions, $V_{sw} = -370$ km/s, $\theta = 120°$ or (cone angle = 60°) and $T_e = 24$ eV, to be compared with the intermediate IMF case (50° < cone angle < 75°) without strahl, and their differences, as shown in Figure 10. As shown in Figure 10c, the data-model comparison shows a <~20% difference in the most of the wake regions, except near-Moon wake region and mainly at the $+Y'$ side. The small difference

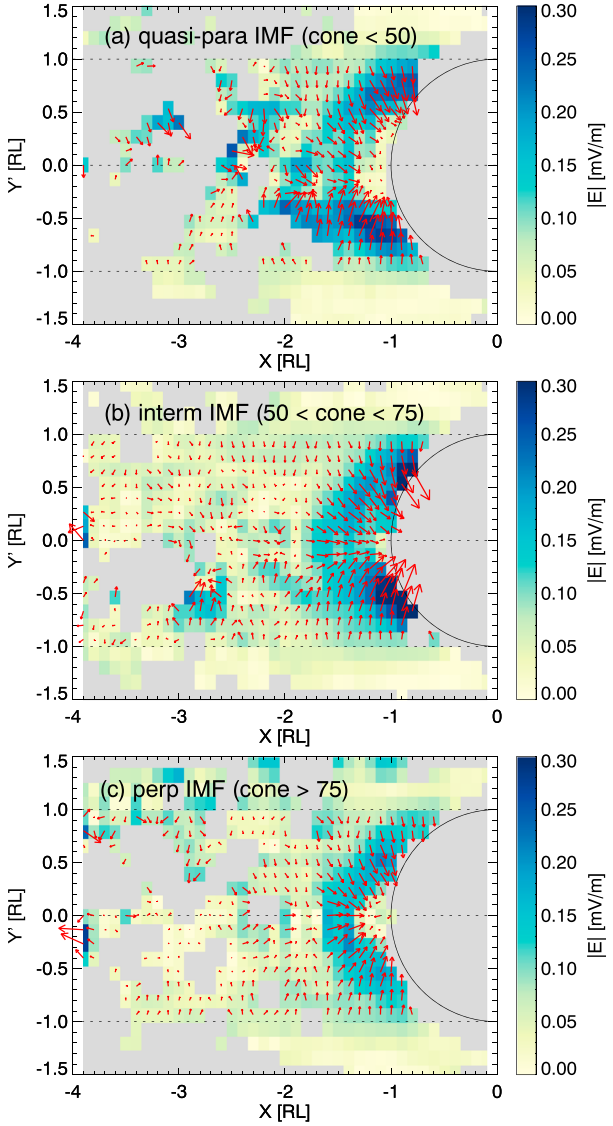

Figure 9. The maps of derived electric fields in the X-Y' plane for cases with no strahl ($1/2.5 < FR < 2.5$): (a) quasi-parallel IMFs (cone angle <50°), (b) intermediate IMFs (50° < cone angle < 75°), and (c) perpendicular IMFs (cone angle > 75°). The color shows the electric field magnitude, and the arrow indicates its direction. The arrow lengths are scaled by electric field magnitudes. IMF = interplanetary magnetic field.

justifies our usage of an electron temperature twice the nominal value, presumably due to the presence of higher energy components (i.e., strahl and halo) in the electron distribution. There are two possible reasons responsible for the disagreement in the near-Moon region. First, the very negative potential in the deep wake filtered out lower-energy electrons and high-energy electrons are more important, which have a much higher effective temperature (a kappa tail) than the Maxwellian core, so that the theory would underpredict the potential. Second, the disagreement at the $+Y'$ side is mostly located in the obstructed region (R1) so that the interaction with the lunar surface probably affects the wake potential structure too.

It is also instructive to compare the electric fields derived from the ARTEMIS data and from our model. The corresponding electric field maps for Figures 10a and 10b are shown in Figures 11a and 11b, respectively. Note that the results in Figure 11a are the same as Figure 9b but in a different display. The modeled electric fields are quite similar to that from the data for $-2 < X < 0$, both the magnitude and the direction, particularly for the $-Y'$ side. The electric field direction is also more perpendicular to the X axis for the $-Y'$ side but more parallel to the X axis for the $+Y'$ side from both the model and data. The separation of $\pm E_y$ is

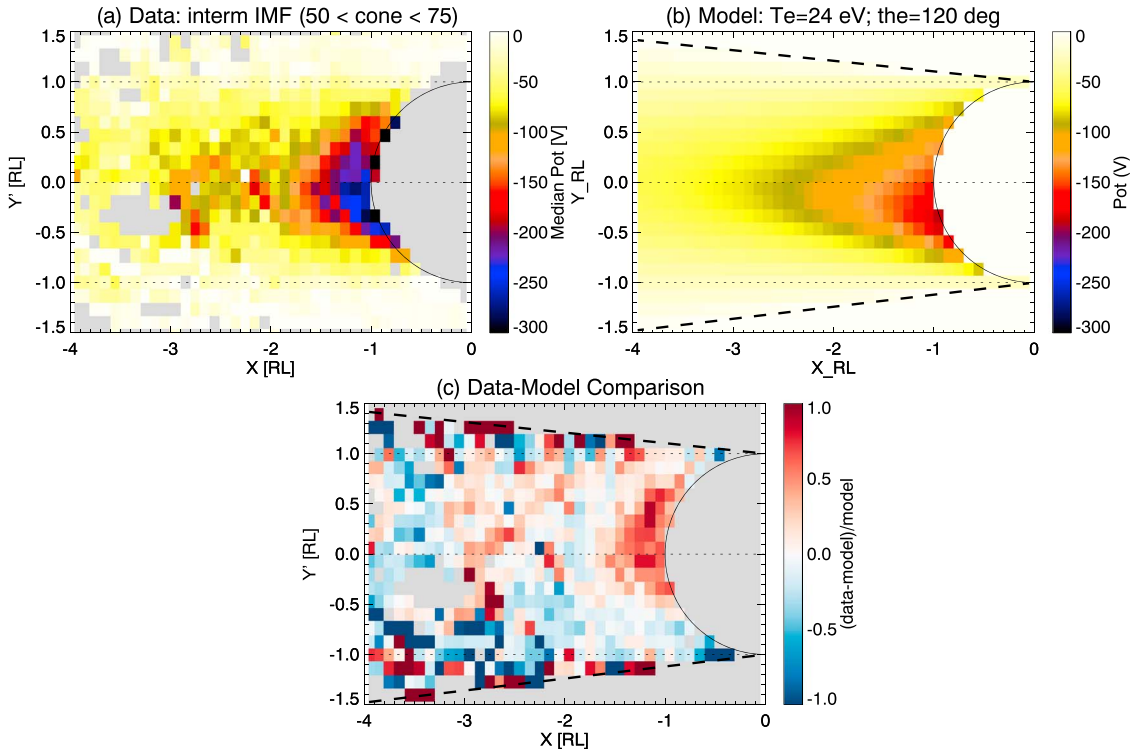

Figure 10. Maps of wake potentials from the data for the intermediate IMF case (a) and the model (b) in the X-Y' plane. (a) is the same as Figure 8b. (c) The relative difference is calculated as (*data-model*)/*model*. The positive values in (c), or the red color, means the data-derived potential is more negative. IMF = interplanetary magnetic field.

shifted to $Y' = \sim -0.2$ (the dotted red lines in Figures 11a and 11b) in both the modeled and data-derived electric fields as well. These agreements demonstrate that our theory of the effects of a tilted IMF on the wake potential structure describes the ARTEMIS data well.

Regarding the $+Y'$ side, although the modeled electric field peaks at large Y' and resembles the data near the Moon, the data-derived electric field has a band of high $|E|$ stretching toward the wake center near $X = -1.5\,R_L$ that is missing from the model. It indicates some physics that are not captured by the model, which is based on the simple gas dynamic theory with several assumptions. This disagreement in the electric field magnitude corresponds to the >50% data-model difference of potentials at the $+Y'$ side in Figure 10c.

We can also compare to previously published computational models of the lunar wake electrostatic potential. In particular, Fatemi (2014) predicted the ambipolar electric field in the lunar wake for parallel and perpendicular IMF conditions with a hybrid plasma model. Under a nominal solar wind condition with a velocity of 400 km/s, an electron temperature of 15 eV, and a density of 5 cm^{-3}, the simulated ambipolar electric field magnitude is roughly 0.1–0.3 mV/m within the rarefaction region, reaching a maximum of <0.6 mV/m close to the lunar surface for a perpendicular IMF (Figure 4.11 in Fatemi, 2014). The simulated ambipolar electric fields are in a good agreement with our calculated electric fields in Figures 7 and 9.

5. Discussion and Conclusions

In this study, field-aligned potentials are derived from ARTEMIS electron and magnetic field observations by comparing the field-aligned electron distributions inside and outside of the wake, following the case study by Halekas et al. (2011b). We applied this methodology to data collected by the ARTEMIS probes from mid-2011 to the end of 2018 and statistically analyze and map the lunar wake potentials in the plane of the IMF and the solar wind velocity. As predicted by the theory of 1-D plasma expansion into a vacuum, the wake potential drops are larger for higher solar wind electron temperatures, as more electrons are distributed in the high-energy tail to set up electron-ion charge separation, leading to a larger ambipolar electric field. The

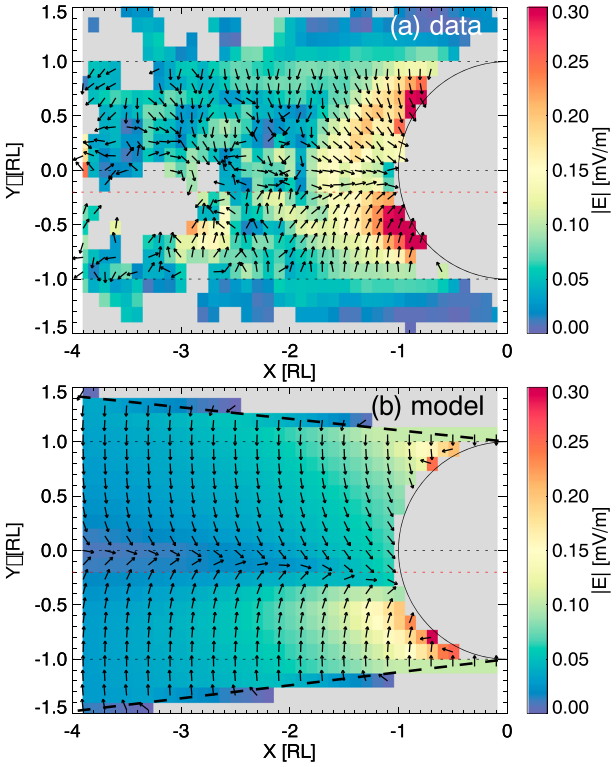

Figure 11. (a, b) Maps of electric fields derived from Figures 10a and 10b in the X-Y' plane, respectively. (a) is the same as Figure 9b but with a different display. The color shows the electric field magnitude, and the arrow with a uniform length indicates its direction.

wake potential is more extended for faster solar wind speeds, as the expansion time is shorter for the same downstream convection distance.

We have also derived a model of the lunar wake potential in a 2-D plane for a tilted IMF, that is, the IMF neither perpendicular nor parallel to the solar wind velocity, adapting the methodology from Hutchinson (2012). The analytical solutions predict an asymmetry in the wake potential for a tilted IMF, caused by different plasma expansion times for the two sides of the wake. By changing the "effective" lunar radius for 2-D planes away from the equator, the potentials can be obtained in 3-D. This wake potential asymmetry is confirmed by data, where we examine and compare the lunar wake potential structures for more perpendicular IMF and more parallel IMF. For more perpendicular IMF, the lunar wake potentials are quite symmetric to the X axis. In contrast, when the IMF is tilted, or more parallel, the wake potential pattern shifts to the $-Y'$ side, in agreement with our model. Moreover, the derived ambipolar electric fields from ARTEMIS data and our model, as well as from a hybrid model (Fatemi, 2014), show good agreement in directions and magnitudes, albeit with some discrepancies in the $+Y'$ side, probably because of some physics not captured by our simple model.

Lastly, as indicated in the case study by Halekas et al. (2011b), the electron strahl population caused a net potential difference as the spacecraft crossed the wake. We further investigate this issue by comparing wake potentials for large (strahl case) and small (nonstrahl case) field-aligned electron FRs under perpendicular IMF, shown in Figure 12. For the nonstrahl case, the wake potential is rather symmetric, as indicated by Figures 6b and 6d, as well as the averaged potential profile against Y', as displayed in Figure 12b. In contrast, the wake potential exhibits a large potential difference near the center of the wake for the strahl case, as shown in Figure 12a, also indicated by Figures 6a and 6c. As a large electric field is not expected near the wake center, rather, the potential difference of ~50 V near $Y' = 0$ in Figure 12a should be considered as the potential difference between our two zero-potential reference points for each side of the wake, by matching the potential at the wake center.

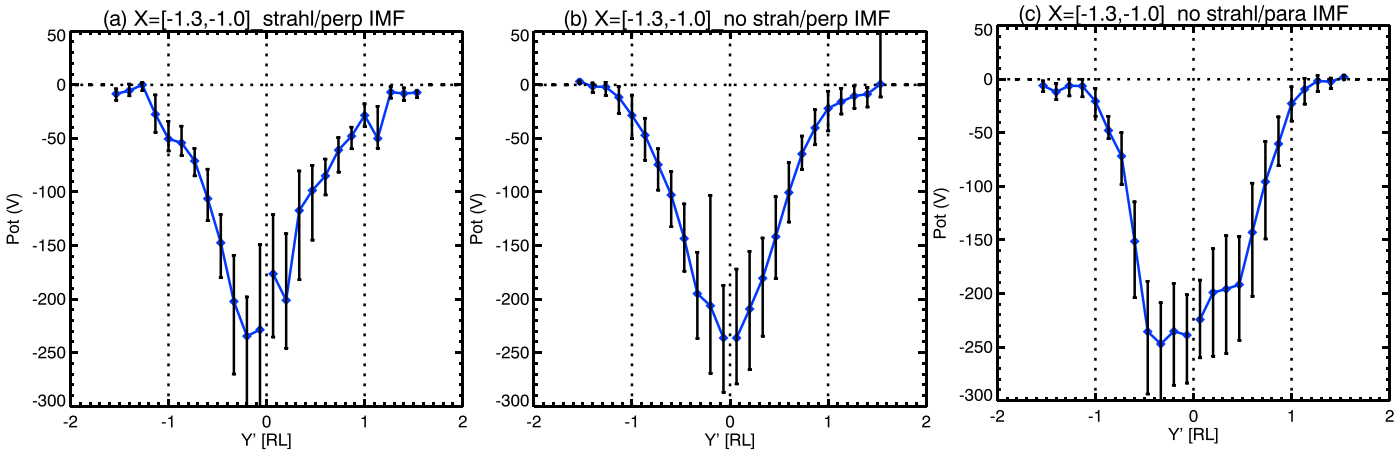

Figure 12. The averaged potential over $X = [-1.3, -1.0]$ and $Z = [-0.5, 0.5]$ against Y' for the strahl case (a) and the nonstrahl case (b) under perpendicular IMFs, corresponding to the data within the two dashed lines in Figures 6a and 6b, respectively. (c) The averaged potential against Y' for quasi-parallel IMFs under a nonstrahl condition, corresponding to the data within the two dashed lines in Figures 8a. The vertical bars indicate quartiles of each bin. IMF = interplanetary magnetic field.

The interpretation of this net potential difference is intriguing. To compare with the potential asymmetry introduced by the IMF tilting, Figure 12c shows the averaged potential for parallel IMF under a nonstrahl condition, which shows little potential jump near $Y' = 0$ and only exhibits a shift of the minimum potential to $Y' = -0.4$, with the potentials outside of both sides of the wake near zero. This agrees with our model of a potential shifting but no net potential difference is produced across the wake. In contrast, the net potential difference near $Y' = 0$ for the strahl case (Figure 12a) probably means that our choice of zero potential reference for the $+Y'$ side is not optimized. This is probably also why the potential is still slowly rising from $Y' = 1$ to $Y' = 1.5$ in Figure 12a. According to the expansion theory, the expansion fronts (E_1 and E_2 in Figure 2a) should be within $|Y'| < 1.2R_L$ for $X > -2R_L$, upstream of which the solar wind plasma should be undisturbed. The results of the strahl case, however, indicate a faster upstreamward propagation of plasma disturbance from the wake expansion than the theory predicts, especially considering the effects from fast-traveling electrons, so that our zero-potential locations are probably not set far enough from the wake edge. Meanwhile, it is not practical either to a zero potential much further from the wake for the following reasons: (1) This may significantly reduce our sampling statistics as it requires ARTEMIS samples at a larger distance from the X axis, while it crosses the wake; (2) further away from the wake, there is a higher chance that the upstream solar wind conditions vary with time (in particular, the reference electron spectrum might be different from the source of the wake electron populations); and (3) the delta potential per spatial step of the spacecraft, that is, the electric field, outside of the lunar shadow that compensates the net potential difference (a few tens of volts) might be too small for the electrostatic analyzer instrument to detect with its current energy resolution. In summary, we interpret the net potential difference across the wake in the presence of the solar wind strahl population to be a result of our zero-potential reference locations not being optimized, which also indicates that the disturbance from the wake plasma expansion extends to further into the upstream plasma than the simple plasma-expansion theory predicts.

Appendix A: Derivation for Plasma Expansion Theory for a Tilted IMF

As illustrated in Figure 1, the tangent point $T(X_t, Y_t)$ is located at

$$X_t = R_L \cos(\theta + \pi/2) = -R_L \cos\theta, \tag{A1}$$

$$Y_t = R_L \sin(\theta + \pi/2) = R_L \sin\theta. \tag{A2}$$

Then, L_1 and L_2 can be written as follows:

$$L_1 : y = x\tan\theta + R_L/\cos\theta, \tag{A3}$$

$$L_2 : y = -x/\tan\theta. \tag{A4}$$

Assuming an undisturbed upstream plasma density n_0, from $R_L \rightarrow -R_L$, the expansion time is $t_1 = X_1/V_{sw}$ and the traveling distance is $S_1 = (R_L - y)/\sin\theta$, which are then substituted into equations (1) and (3), giving

$$\phi_1/(T_e/e) = -1 - \frac{1}{u}\frac{R_L - y}{x\sin\theta + (R_L - y)\cos\theta}, \tag{A5}$$

$$n_1/n_0 = exp(\frac{\phi_1}{T_e/e}), \tag{A6}$$

$$E_1 : y = R_L + \frac{xu\sin\theta}{1 + u\cos\theta}, \tag{A7}$$

where E_1 is the expansion front where $\phi_1 = 0$ at $S/(C_s t_1) + 1 = 0$.

Similarly, from $-R_L \rightarrow R_L$, the expansion time is $t_2 = X_2/V_{sw}$ and the traveling distance is $S_2 = (R_L + y)/\sin\theta$, which gives

$$\phi_2/(T_e/e) = -1 - \frac{1}{u}\frac{R_L + y}{x\sin\theta - (R_L + y)\cos\theta}, \tag{A8}$$

$$n_2/n_0 = exp(\frac{\phi_2}{T_e/e}), \tag{A9}$$

$$E_2 : y = -R_L - \frac{xu\sin\theta}{1 - u\cos\theta}, \tag{A10}$$

where E_2 is the expansion front where $\phi_2 = 0$ at $S/(C_s t_2) + 1 = 0$.

For R1, there is only plasma expanding from R_L to the lunar surface such that

$$\phi/(T_e/e) = \phi_1/(T_e/e) = -1 - \frac{1}{u}\frac{R_L - y}{x\sin\theta + (R_L - y)\cos\theta}. \tag{A11}$$

For R2, there is only plasma expanding from $-R_L \rightarrow R_L$ such that

$$\phi/(T_e/e) = \phi_2/(T_e/e) = -1 - \frac{1}{u}\frac{R_L + y}{x\sin\theta - (R_L + y)\cos\theta}. \tag{A12}$$

For R3, there are plasma entering from both sides. Following Hutchinson (2012), there is a density of n_1 traveling from $R_L \rightarrow -R_L$ and a density of n_2 traveling from $-R_L \rightarrow R_L$. Although not rigorously justified, it can be approximated by $n_{total} = n_1 + n_2$, the same as Hutchinson (2012), then we have

$$\phi = \ln(n_{total}/n_0) = \ln(n_1/n_0 + n_2/n_0). \tag{A13}$$

Substituting equations (A5), (A6), (A8), and (A9) into (A13), we have the potential for R3:

$$\phi/(T_e/e) = -1 + \ln\left\{\exp\left[-\frac{1}{u}\frac{R_L - y}{x\sin\theta + (R_L - y)\cos\theta}\right] + \exp\left[-\frac{1}{u}\frac{R_L + y}{x\sin\theta - (R_L + y)\cos\theta}\right]\right\}. \tag{A14}$$

Acknowledgments
S. X., A. R. P., and J. S. H. gratefully acknowledge support from NASA's Solar System Exploration Research Virtual Institute (SSERVI), grants NNX14AG16A and NNX15AH15A. The ARTEMIS mission is funded and operated under NASA grant NAS5-02099, and we specifically acknowledge K.-H. Glassmeier, U. Auster, and W. Baumjohann for the use of FGM data provided under the lead of the Technical University of Braunschweig and with financial support through the German Ministry for Economy and Technology and the German Center for Aviation and Space (DLR), contract 50 OC 0302. All ARTEMIS data necessary for this study are publicly available at the ARTEMIS website (http://artemis.ssl.berkeley.edu). Data access and processing was done using SPEDAS V3.1; see Angelopoulos et al. (2019).

References

Angelopoulos, V. (2011). The ARTEMIS mission. *Space Science Reviews*, *165*, 3–25. https://doi.org/10.1007/s11214-010-9687-2
Angelopoulos, V., Cruce, P., Drozdov, A., Grimes, E., Hatzigeorgiu, N., King, D., et al. (2019). The Space Physics Environment Data Analysis System (SPEDAS). *Space Science Reviews*, *215*(1), 9.

Auster, H., Glassmeier, K., Magnes, W., Aydogar, O., Baumjohann, W., Constantinescu, D., et al. (2008). The THEMIS fluxgate magnetometer. *Space Science Reviews*, *141*(1-4), 235–264.

Birch, P. C., & Chapman, S. C. (2002). Two dimensional particle-in-cell simulations of the lunar wake. *Physics of Plasmas*, *9*, 1785–1789. https://doi.org/10.1063/1.1467655

Bonnell, J., Mozer, F., Delory, G., Hull, A., Ergun, R., Cully, C., et al. (2009). The electric field instrument (EFI) for THEMIS. In *The THEMIS mission* (pp. 303–341). New York, NY: Springer.

Chao, J., Wu, D., Lin, C.-H., Yang, Y.-H., Wang, X., Kessel, M., et al. (2002). *Models for the size and shape of the Earth's magnetopause and bow shock, Cospar Colloquia Series* (Vol. 12, pp. 127–135). New York: Elsevier.

Colburn, D. S., Currie, R. G., Mihalov, J. D., & Sonett, C. P. (1967). Diamagnetic solar-wind cavity discovered behind Moon. *Science*, *158*(3804), 1040–1042.

Dhanya, M. B., Bhardwaj, A., Futaana, Y., Barabash, S., Alok, A., Wieser, M., et al. (2016). Characteristics of proton velocity distribution functions in the near-lunar wake from Chandrayaan-1/SWIM observations. *Icarus*, *271*, 120–130.

Dhanya, M., Bhardwaj, A., Futaana, Y., Fatemi, S., Holmström, M., Barabash, S., et al. (2013). Proton entry into the near-lunar plasma wake for magnetic field aligned flow. *Geophysical Research Letters*, *40*, 2913–2917. https://doi.org/10.1002/grl.50617

Farrell, W. M., Kaiser, M. L., Steinberg, J. T., & Bale, S. D. (1998). A simple simulation of a plasma void: Applications to wind observations of the lunar wake. *Journal of Geophysical Research*, *103*, 23,653–23,660. https://doi.org/10.1029/97JA03717

Fatemi, T. (2014). Kinetic modeling of the solar wind plasma interaction with the Moon (PhD thesis).

Fatemi, S., Holmström, M., Futaana, Y., Barabash, S., & Lue, C. (2013). The lunar wake current systems. *Geophysical Research Letters*, *40*, 17–21. https://doi.org/10.1029/2012GL054635

Fatemi, S., Poppe, A. R., Delory, G. T., & Farrell, W. M. (2017). Amitis: A 3D GPU-based hybrid-PIC model for space and plasma physics. *Journal of Physics: Conference Series*, *837*, 012017. IOP Publishing.

Futaana, Y., Barabash, S., Wieser, M., Holmström, M., Bhardwaj, A., Dhanya, M. B., et al. (2010). Protons in the near-lunar wake observed by the sub-keV atom reflection analyzer on board chandrayaan-1. *Journal of Geophysical Research*, *115*, A10248. https://doi.org/10.1029/2010JA015264

Gurevich, A., & Pitaevskii, L. (1975). Non-linear dynamics of a rarefied ionized gas. *Progress in Aerospace Sciences*, *16*, 227–272.

Gurevich, A. V., Pitaevskii, L., & Smirnova, V. (1969). Ionospheric aerodynamics. *Space Science Reviews*, *9*(6), 805–871.

Halekas, J., Angelopoulos, V., Sibeck, D., Khurana, K., Russell, C., Delory, G., et al. (2011b). First results from ARTEMIS, a new two-spacecraft lunar mission: Counter-streaming plasma populations in the lunar wake. *Space Science Reviews*, *165*, 93–107. The ARTEMIS Mission, Springer.

Halekas, J., Bale, S., Mitchell, D., & Lin, R. (2005). Electrons and magnetic fields in the lunar plasma wake. *Journal of Geophysical Research*, *110*, A07222. https://doi.org/10.1029/2004JA010991

Halekas, J., Mitchell, D., Lin, R., Hood, L., Acuña, M., & Binder, A. (2002). Evidence for negative charging of the lunar surface in shadow. *Geophysical Research Letters*, *29*(10), 1435. https://doi.org/10.1029/2001GL014428

Halekas, J., Poppe, A., & McFadden, J. (2014). The effects of solar wind velocity distributions on the refilling of the lunar wake: ARTEMIS observations and comparisons to one-dimensional theory. *Journal of Geophysical Research: Space Physics*, *119*, 5133–5149. https://doi.org/10.1002/2014JA020083

Halekas, J., Saito, Y., Delory, G., & Farrell, W. (2011a). New views of the lunar plasma environment. *Planetary and Space Science*, *59*(14), 1681–1694.

Harnett, E. M., & Winglee, R. M. (2002). 2.5D particle and MHD simulations of mini-magnetospheres at the Moon. *Journal of Geophysical Research*, *107*(A12), 1421. https://doi.org/10.1029/2002JA009241

Holmström, M., Fatemi, S., Futaana, Y., & Nilsson, H. (2012). The interaction between the Moon and the solar wind. *Earth, Planets and Space*, *64*, 237–245. https://doi.org/10.5047/eps.2011.06.040

Hutchinson, I. (2012). Electron velocity distribution instability in magnetized plasma wakes and artificial electron mass. *Journal of Geophysical Research*, *117*, A03101. https://doi.org/10.1029/2011JA017119

Hutchinson, I. (2013). Near-lunar proton velocity distribution explained by electrostatic acceleration. *Journal of Geophysical Research: Space Physics*, *118*, 1825–1827. https://doi.org/10.1002/jgra.50277

Kallio, E. (2005). Formation of the lunar wake in quasi-neutral hybrid model. *Geophysical Research Letters*, *32*, L06107. https://doi.org/10.1029/2004GL021989

Kimura, S., & Nakagawa, T. (2008). Electromagnetic full particle simulation of the electric field structure around the Moon and the lunar wake. *Earth, Planets and Space*, *60*, 591–599.

McFadden, J., Carlson, C., Larson, D., Ludlam, M., Abiad, R., Elliott, B., et al. (2008). The THEMIS ESA plasma instrument and in-flight calibration. *Space Science Reviews*, *141*(1-4), 277–302.

Nakagawa, T. (2013). Ion entry into the wake behind a nonmagnetized obstacle in the solar wind: Two-dimensional particle-in-cell simulations. *Journal of Geophysical Research: Space Physics*, *118*, 1849–1860. https://doi.org/10.1002/jgra.50129

Ness, N. F. (1972). Interaction of the solar wind with the Moon, *Solar-Terrestrial Physics/1970* (pp. 347–393). Dordrecht: Springer.

Ness, N. F., Behannon, K. W., Taylor, H. E., & Whang, Y. C. (1968). Perturbations of the interplanetary magnetic field by the lunar wake. *Journal of Geophysical Research*, *73*(11), 3421–3440.

Nishino, M. N., Fujimoto, M., Maezawa, K., Saito, Y., Yokota, S., Asamura, K., et al. (2009a). Solar-wind proton access deep into the near-Moon wake. *Geophysical Research Letters*, *36*, L16103. https://doi.org/10.1029/2009GL039444

Nishino, M. N., Fujimoto, M., Saito, Y., Yokota, S., Kasahara, Y., Omura, Y., et al. (2010). Effect of the solar wind proton entry into the deepest lunar wake. *Geophysical Research Letters*, *37*, L12106. https://doi.org/10.1029/2010GL043948

Nishino, M. N., Harada, Y., Saito, Y., Tsunakawa, H., Takahashi, F., Yokota, S., et al. (2017). Kaguya observations of the lunar wake in the terrestrial foreshock: Surface potential change by bow-shock reflected ions. *Icarus*, *293*, 45–51.

Nishino, M. N., Maezawa, K., Fujimoto, M., Saito, Y., Yokota, S., Asamura, K., et al. (2009b). Pairwise energy gain-loss feature of solar wind protons in the near-Moon wake. *Geophysical Research Letters*, *36*, L12108. https://doi.org/10.1029/2009GL039049

Ogilvie, K. W., Steinberg, J. T., Fitzenreiter, R. J., Owen, C. J., Lazarus, A. J., Farrell, W. M., & Torbert, R. B. (1996). Observations of the lunar plasma wake from the WIND spacecraft on December 27, 1994. *Geophysical Research Letters*, *23*, 1255–1258. https://doi.org/10.1029/96GL01069

Poppe, A., Fatemi, S., Halekas, J., Holmström, M., & Delory, G. (2014). ARTEMIS, observations of extreme diamagnetic fields in the lunar wake. *Geophysical Research Letters*, *41*, 3766–3773. https://doi.org/10.1002/2014GL060280

Russell, C. T., Luhmann, J. G., & Strangeway, R. J. (2016). *Space physics: An introduction*. Cambridge: Cambridge University Press.

Samir, U., Wright, JrK., & Stone, N. H. (1983). The expansion of a plasma into a vacuum: Basic phenomena and processes and applications to space plasma physics. *Reviews of Geophysics*, *21*(7), 1631–1646.

Schubert, G., & Lichtenstein, B. R. (1974). Observations of Moon-plasma interactions by orbital and surface experiments. *Reviews of Geophysics and Space Physics*, *12*, 592–626. https://doi.org/10.1029/RG012i004p00592

Trávnícek, P., Hellinger, P., Schriver, D., & Bale, S. D. (2005). Structure of the lunar wake: Two-dimensional global hybrid simulations. *Geophysical Research Letters*, *32*, L06102. https://doi.org/10.1029/2004GL022243

Umeda, T., Kimura, T., Togano, K., Fukazawa, K., Matsumoto, Y., Miyoshi, T., et al. (2011). Vlasov simulation of the interaction between the solar wind and a dielectric body. *Physics of Plasmas*, *18*(1), 012908. https://doi.org/10.1063/1.3551510

Wang, X.-D., Bian, W., Wang, J.-S., Liu, J.-J., Zou, Y.-L., Zhang, H.-B., et al. (2010). Acceleration of scattered solar wind protons at the polar terminator of the Moon: Results from Chang'E-1/SWIDs. *Geophysical Research Letters*, *37*, L07203. https://doi.org/10.1029/2010GL042891

Wang, Y.-C., Müller, J., Ip, W.-H., & Motschmann, U. (2011). A 3D hybrid simulation study of the electromagnetic field distributions in the lunar wake. *Icarus*, *216*, 415–425. https://doi.org/10.1016/j.icarus.2011.09.021

Whipple, E. C. (1981). Potentials of surfaces in space. *Reports on Progress in Physics*, *44*(11), 1197.

Wiehle, S., Plaschke, F., Motschmann, U., Glassmeier, K.-H., Auster, H. U., Angelopoulos, V., et al. (2011). First lunar wake passage of ARTEMIS: Discrimination of wake effects and solar wind fluctuations by 3D hybrid simulations. *Planetary and Space Science*, *59*, 661–671. https://doi.org/10.1016/j.pss.2011.01.012

Xie, L., Li, L., Zhang, Y., & De Zeeuw, D. L. (2013). Three-dimensional MHD simulation of the lunar wake. *Science China Earth Sciences*, *56*(2), 330–338.

Xu, X., Wong, H.-C., Ma, Y., Wang, Y., Zuo, P., Zhou, M., et al. (2017). Anomalously high rate refilling in the near lunar wake caused by the Earth's bow shock. *Journal of Geophysical Research: Space Physics*, *122*, 9102–9114. https://doi.org/10.1002/2016JA023505

Zhang, H., Khurana, K., Kivelson, M., Angelopoulos, V., Wan, W., Liu, L., et al. (2014). Three-dimensional lunar wake reconstructed from ARTEMIS data. *Journal of Geophysical Research: Space Physics*, *119*, 5220–5243. https://doi.org/10.1002/2014JA020111

Zhang, H., Khurana, K. K., Zong, Q.-G., Kivelson, M. G., Hsu, T.-S., Wan, W. X., et al. (2012). Outward expansion of the lunar wake: ARTEMIS observations. *Geophysical Research Letters*, *39*, L18104. https://doi.org/10.1029/2012GL052839